Supporting information

Manipulating electronic configuration of Fe-N_4 sites by electron-withdrawing/donating strategy with improved oxygen electroreduction performance

Yonggan Wu,[†,a] Xiannong Tang,[†,a] Fangjun Zhang,[b] Longbin Li,[a] Weijuan Zhai,[a] Bingyu Huang,[a] Ting Hu,[c] Dirk Lützenkirchen-Hecht,[d] Kai Yuan,[*,a] and Yiwang Chen[*,a,e]

[a.] Institute of Polymers and Energy Chemistry (IPEC), College of Chemistry and Chemical Engineering, Nanchang University, 999 Xuefu Avenue, Nanchang 330031, China. E-mail: kai.yuan@ncu.edu.cn; ywchen@ncu.edu.cn

[b.] School of Future Technology, Nanchang University, 999 Xuefu Avenue, Nanchang 330031, China

[c.] School of Materials Science and Engineering, Nanchang University, 999 Xuefu Avenue, Nanchang 330031, China

[d.] Faculty of Mathematics and Natural Sciences-Physics Department, Bergische Universität Wuppertal, Gauss-Str. 20, D-42119 Wuppertal, Germany

[e.] Institute of Advanced Scientific Research (iASR), Key Lab of Fluorine and Silicon for Energy Materials and Chemistry of Ministry of Education, Jiangxi Normal University, 99 Ziyang Avenue, Nanchang 330022, China

[†] These authors contributed equality to this work.

Experimental section

Materials. Zinc nitrate hexahydrate (99.9%), 2-methylimidazole (98%), Iron acetylacetonate (98%), Zinc acetate (99%) and Polyvinyl alcohol (M_W=145000) were obtained from Sigma Aldrich. Boric acid was bought from Xilong Chemical Technology Co., Ltd. Nafion (5% w/w in water and 1-propanol) and commercial Pt/C (20 wt% Pt) were obtained from Alfa Aesar. RuO_2 (99.9% trace metal basis) was obtained from Sigma Aldrich. KOH (85%) and H_2SO_4 (98%) were purchased from Sinopharm Chemical Reagent Co., Ltd (China). Carbon paper was obtained from Hesen Electric Inc. Shanghai, and carbon cloth substrate was obtained from WOS 1002, CeTech. All the chemicals are analytical grade and used without further purification.

Synthesis of Zn/Fe-ZIF. Typically, 2-methylimidazole (2627 mg, 32 mmol) was dissolved in 30 mL deionized water under stirring in a break to form solution A. $Zn(NO_3)_2{\cdot}6H_2O$ (1190 mg, 4 mmol) and $Fe(acac)_3$ (88 mg 0.25 mmol) were dissolved in a mixed solution containing 10 mL ethanol and 20 mL deionized water under ultrasound in a break to form a homogeneous solution B. Then, solution A was subsequently added into solution B under vigorous stirring for 1 h at room temperature. The above solution was left undisturbed at room temperature for 12 h. The precipitate was washed with 50% ethanol solution and separated by centrifugation. After freeze-drying, the yellow Zn/Fe-ZIF precursor was finally obtained.

Synthesis of Fe-SA/NC. The powder of Zn/Fe-ZIF was transferred into a ceramic boat and placed in a tube furnace. The sample was heated to 900 °C under flowing nitrogen gas for 3 h with a heating rate of 5 °C min^{-1}, and then naturally cooled to room temperature. The resultant products were leached with 0.5 M H_2SO_4 for 24 h at 80 °C, and washed with deionized water, and then dried under vacuum. The obtained products were named Fe-SA/NC.

Synthesis of Fe-SA/BNC. Fe-SA/BNC-(X)-900: A certain amount of Fe-SA/NC and H_3BO_3 (with Fe-SA/NC to H_3BO_3 mass ratios of X, X= 2:1, 5:1, 10:1) were added to 10 mL ethanol to form a suspension. The above suspension was sonicated for 1 h, then stirred at room temperature until dried. The obtained powder was transferred into a ceramic boat and placed in a tube furnace. The sample was heated to 900 °C under flowing nitrogen gas for 1 h with a heating rate of 5 °C min^{-1}, and then naturally cooled to room temperature.

Fe-SA/BNC-(5:1)-Y: A certain amount of Fe-SA/NC and H_3BO_3 (with Fe-SA/NC to H_3BO_3 mass ratios of 5:1) were added to 10 mL ethanol to form a suspension. The above suspension was sonicated for 1 h, then stirred at room temperature until dried. The obtained powder was transferred into a ceramic boat and placed in a tube furnace. The sample was heated to different temperature Y (Y= 800 °C, 900 °C, 1000 °C) under flowing nitrogen gas for 1 h with a heating rate of 5 °C min^{-1}, and then naturally cooled to room temperature.

Fe-SA/BNC-(5:1)-900 was the optimal sample, abbreviated as Fe-SA/BNC.

Synthesis of ZIF-8. The synthesis of ZIF-8 was similar to the above method of Zn/Fe-ZIF except for the addition of $Fe(acac)_3$.

Synthesis of NC. The synthesis of NC was similar to the above method of Fe-SA/NC, except that Zn/Fe-ZIF was substituted by ZIF-8.

Synthesis of BNC. The synthesis of BNC was similar to the above method of Fe-SA/BNC except that Fe-SA/NC was substituted by NC.

Characterization

SEM images were collected using a JEOL JSM-7900F. TEM images were collected using a Titan G260-300. The aberration-corrected HAADF-STM measurement was

performed by FEI-Titan Cubed Themis G2 300. ICP-OES was performed on Agilent 5100. The nitrogen adsorption-desorption isotherms were measured at 77 K with a Quantachrome Autosorb-iQ. Powder XRD patterns were obtained by a Bruker-AXS D8 Advance X-ray diffractometer. Raman spectra were obtained on a HORIBA LabRAM HR Raman spectrometer system.

XPS measurements. XPS spectra were recorded on a Thermo Scientific Escalab 250Xi, with an energy resolution of ±0.1 eV, monochromatized Al Kα (1486.6 eV) radiation and a hemispherical sector analyzer were used. The XPS spectra were deconvoluted using Gaussian-Lorentzian functions after the Shirley background subtraction by CasaXPS software, and the integrated peak areas being used to estimate the surface chemical compositions. All XPS spectra were corrected for any charging effects by fixing the C 1s binding energy at 284.4 eV.

XAFS measurements. X-ray absorption spectroscopy (XAS) experiments were carried out at the wiggler beamline BL10 at the DELTA storage ring (Dortmund, Germany) operated with 80-130 mA of 1.5 GeV electrons. Fe K-edge spectra were collected using a Si (111)-channel cut monochromator and gas-filled ionization chambers as detectors for the incoming and the transmitted intensities, and a large area photodiode for the fluorescence photons. For comparison, a metal Fe-foil as well as several Fe-reference compounds such as Fe_2O_3, FeO, and FePc (Fe-phthalocyanine) were measured.

O_2-TPD measurements. O_2-TPD measurements were conducted on the AutoChem II 2920. Samples were pretreated by He flow (30 mL min^{-1}) for 2 h at 200 °C. Then cooling to 50 °C, the O_2 adsorption was performed in O_2 flow (30 mL min^{-1}) for 2 h. Finally, the sample was heated from 50 to 600 °C with a heating rate of 10 °C min^{-1} in He flow (30 mL min^{-1}). Desorbed gas was detected by a thermal conductivity detector (TCD).

Electrochemical measurement

All data were recorded on an AutoLab PGSTAT302Nl with PINE AFMSRCE by a three-electrode cell system. The electrocatalyst was loaded on a rotating disk electrode (RDE) with a geometrical surface area of disk (0.19625 cm^{-2}) or rotating ring-disk electrode (RRDE) with a geometrical surface area of disk (0.2475 cm^{-2}) and platinum ring (0.1866 cm^{-2}) (Pine Research Instrumentation, USA) as working electrode. An Ag/AgCl electrode in 3 M KCl solution was used as the reference electrode (RE). A graphite rod was used as the counter electrode (CE). The electrolyte was 0.1 M KOH aqueous solution and purged of O_2 for 30 min before running tests. All potentials in this study refer to RHE, E (RHE) = E (Ag/AgCl) + 0.059 pH + 0.1976.

Preparation of the working electrode. 10 mg of catalyst was dispersed in 1 mL of a solution containing 855 μL of ethanol and 95 μL of deionized water and 50 μL of 5 wt% Nafion solution and then sonicated for 1 h to form a homogeneous catalyst ink. Next, 10 μL of the catalyst dispersion was pipetted onto a glassy carbon electrode (RDE or RRDE). The catalyst dispersion was dried slowly in air until a uniform catalyst distribution across the electrode surface was obtained.

The ECSA was derived from C_{dl}, which was measured by a series of cyclic voltammetry (CV) scanning in a non-Faradaic potential (1.00-1.10 V vs. RHE) at various scans rates of 1-10 mV s^{-1}. The ECSA was determined by the following equation:

$$ECSA = C_{dl}/C_s$$

where Cs represents the specific capacitance of the total double layer (0.04 mF cm^{-2}).

Linear sweep voltammetry (LSV) curves were recorded at 225–2025 rpm with a scan rate of 10 mV s^{-1} using RDE. The geometric area of the electrode was employed to

normalize the currents to current densities. The limited current density was set as the value of current density at 0.40 V (vs. RHE). The j_k was determined by Koutecky-Levich (K-L) equation:

$$\frac{1}{j} = \frac{1}{j_L} + \frac{1}{j_k} = \frac{1}{B\omega^{1/2}} + \frac{1}{j_K}$$

$$B = 0.62nFC_0D_0^{2/3}V^{-1/6}$$

$$j_k = nFkC_0$$

where j is current density measured from LSV curves, j_L is the diffusion-limited current density, j_k is the kinetic current density, is the angular velocity. B is a constant.

The transferred electrons number (n) was determined by RRDE measurements. The constant ring potential was set at 0.4 V vs. Ag/AgCl during the measurements to oxide intermediates of ORR. According to the results of RRDE experiments, the HO_2^- (%) and the n value can be obtained by the following equations:

$$n = \frac{4 \times I_{Disk}}{I_{Disk} + I_{Ring}/N}$$

$$\%\left(HO_2^-\right) = \frac{200 \times I_{Ring}/N}{I_{Disk} + I_{ring}/N}$$

where I_{Disk} is the disk current, I_{Ring} is the ring current and the N is 0.37.

Zn-air battery tests

Liquid Zn-air battery assembly. It was constructed by pairing catalysts loaded onto a carbon paper with a Zn plate (0.20 mm thickness) in electrolyte. First, the air electrode was prepared by pipetting catalyst dispersion carefully onto the carbon paper (1 mg cm^{-2}) using a pipette. The polished zinc plate was served as the anode, and 6 M KOH solution with 0.2 M zinc acetate as electrolyte.

Flexible solid-state Zn-air battery assembly. The air electrodes were prepared by pipetting catalyst slurry carefully onto the carbon cloth (2 mg cm^{-2}), the anode was

made by a polished Zn plate (0.10 mm thickness), while the PVA/KOH gel was made as the electrolyte. The PVA/KOH gel electrolyte was synthesized as follows: 1.0 g of PVA powder was mixed in 10.0 mL of deionized water under continuous stirring at 95 °C for 1.0 h. Subsequently, 1.0 mL of 18 M KOH with 0.2 M zinc acetate was dropwise added to the above mixed solution and the obtained gel was stirred continuously at the same temperature for 30 min. Finally, PVA/KOH gel was sandwiched between the Zn plate and the as-prepared air electrode to assemble the flexible solid-state Zn-air battery.

Battery tests were carried out at room temperature under an ambient atmosphere with a CHI760E or a LAND CT2001A. The specific capacity can be obtained by normalizing the weight of utilized Zn.

Supporting Figures and Table

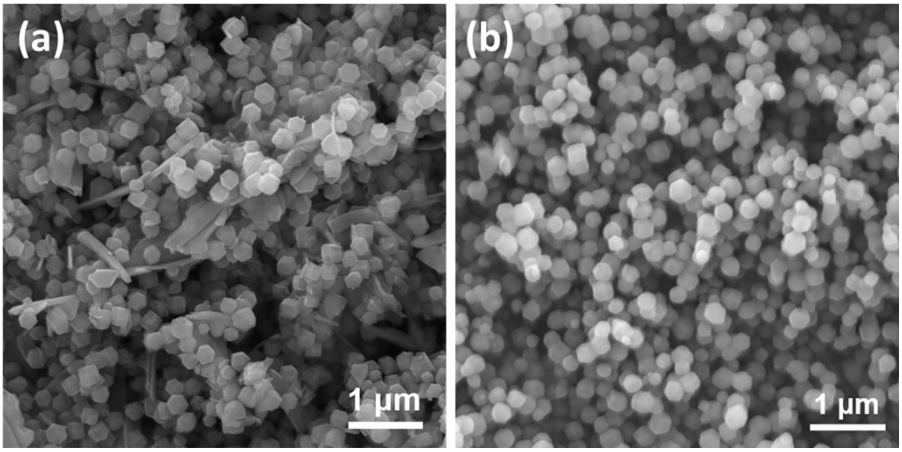

Fig. S1. (a) SEM image of ZIF-8. (b) SEM image of Zn/Fe-ZIF.

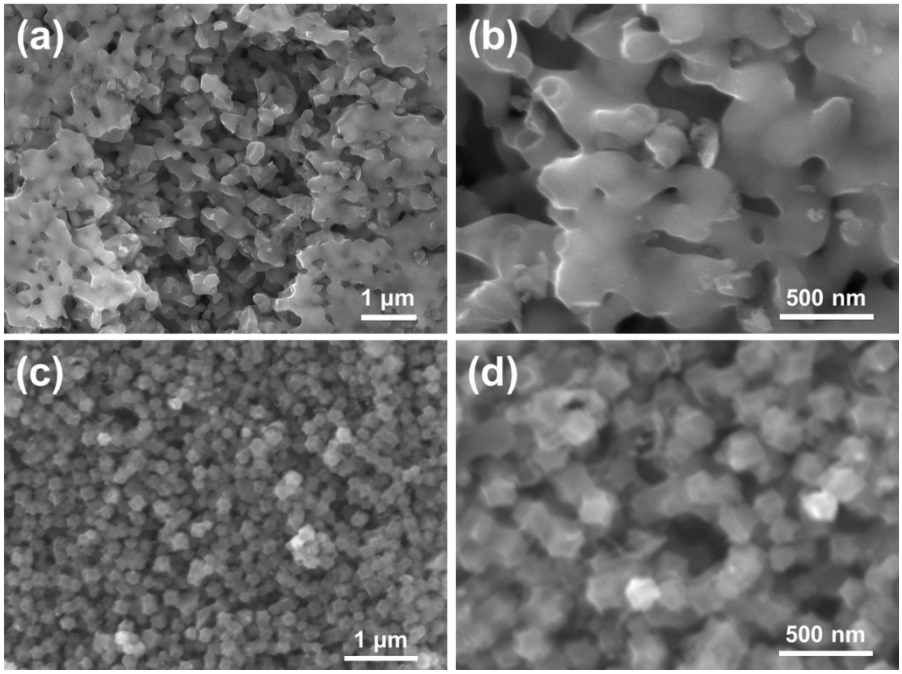

Fig. S2. (a, b) SEM images of NC. (c, d) SEM images of Fe-SA/NC.

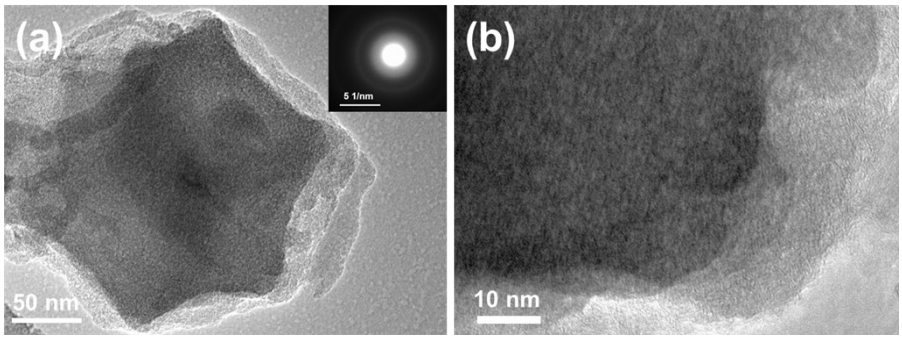

Fig. S3. (a) TEM image and SAED pattern of Fe-SA/NC. (b) HRTEM image of Fe-SA/NC.

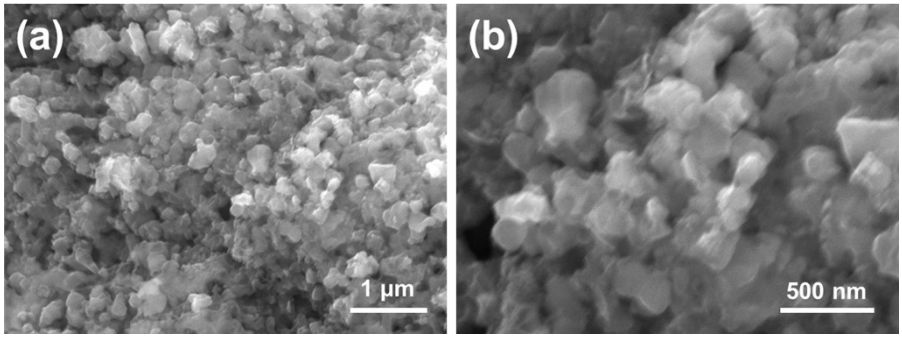

Fig. S4. (a, b) SEM images of BNC.

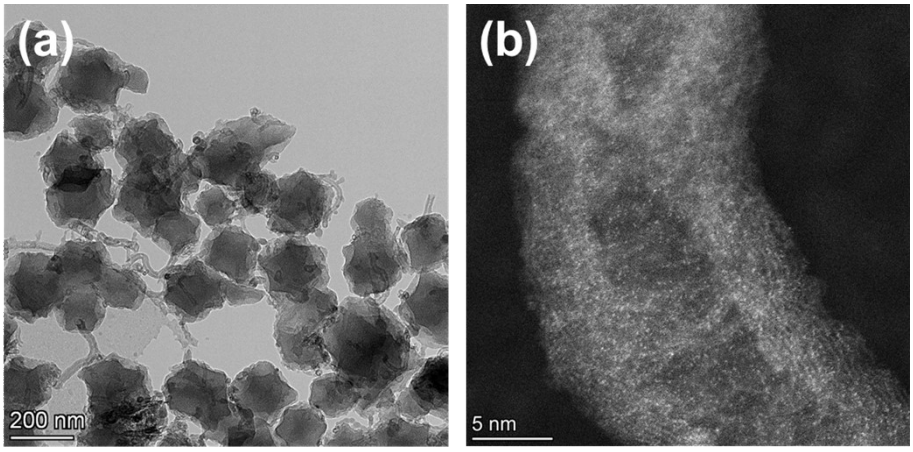

Fig. S5. (a) TEM image of Fe-SA/BNC. (b) Aberration-corrected HAADF-STEM image of Fe-SA/BNC, focusing on carbon nanotubes.

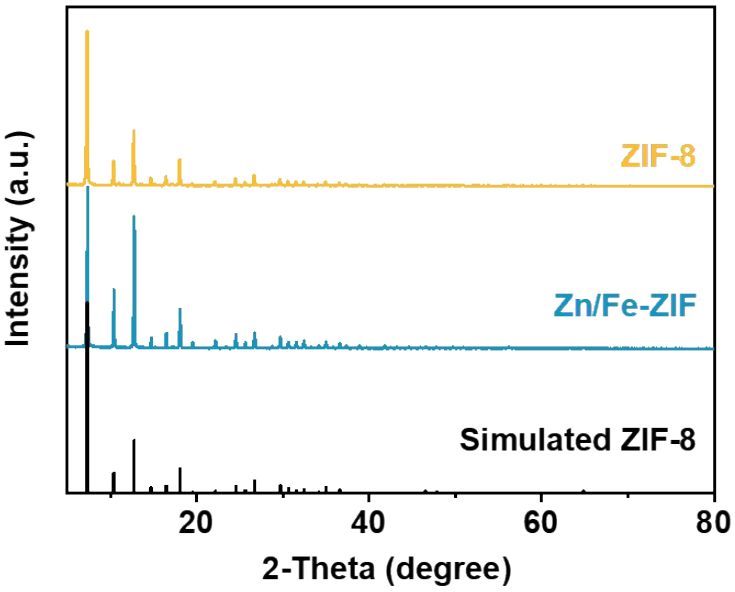

Fig. S6. XRD patterns of ZIF-8, Zn/Fe-ZIF and simulated ZIF-8.

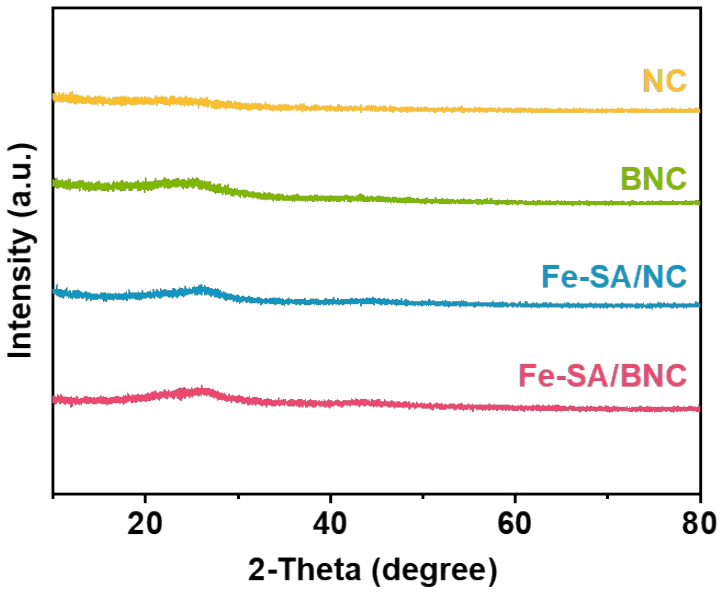

Fig. S7. XRD patterns of NC, BNC, Fe-SA/NC and Fe-SA/BNC.

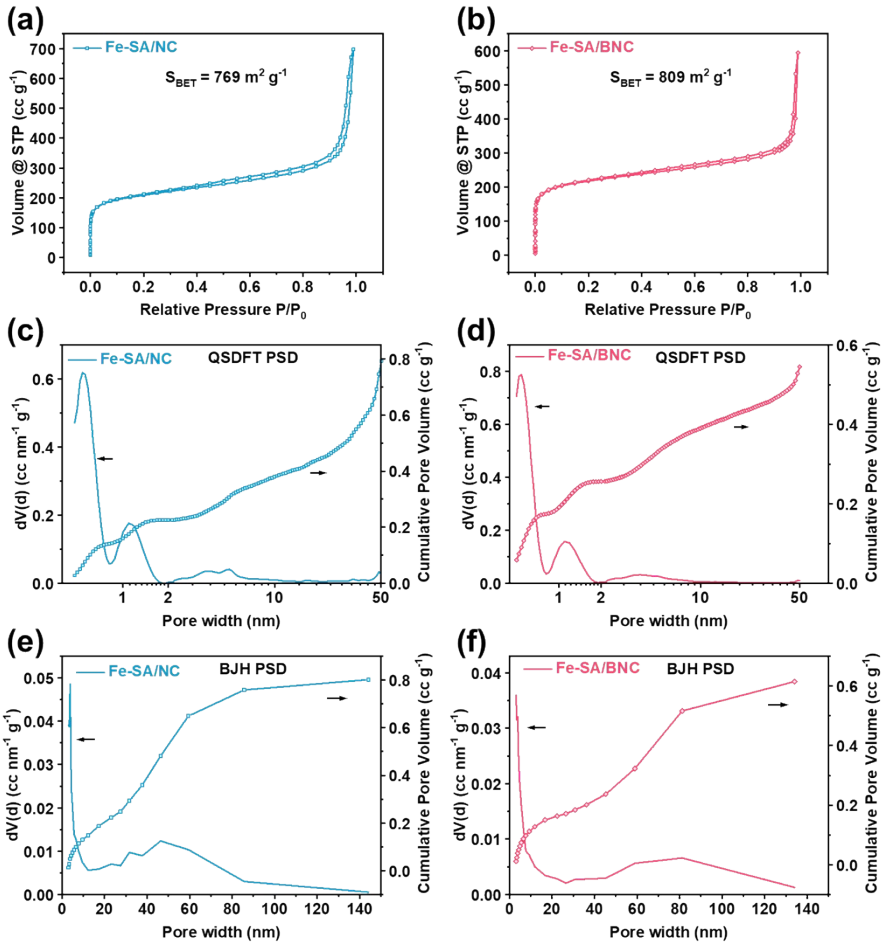

Fig. S8. N_2 adsorption and desorption isotherms of (a) Fe-SA/NC and (b) Fe-SA/BNC. Pore size distribution (PSD) estimated by quenched solid density functional theory (QSDFT) method for (c) Fe-SA/NC and (d) Fe-SA/BNC. PSD estimated by Barrett-Joyner-Halenda (BJH) method for (e) Fe-SA/NC and (f) Fe-SA/BNC.

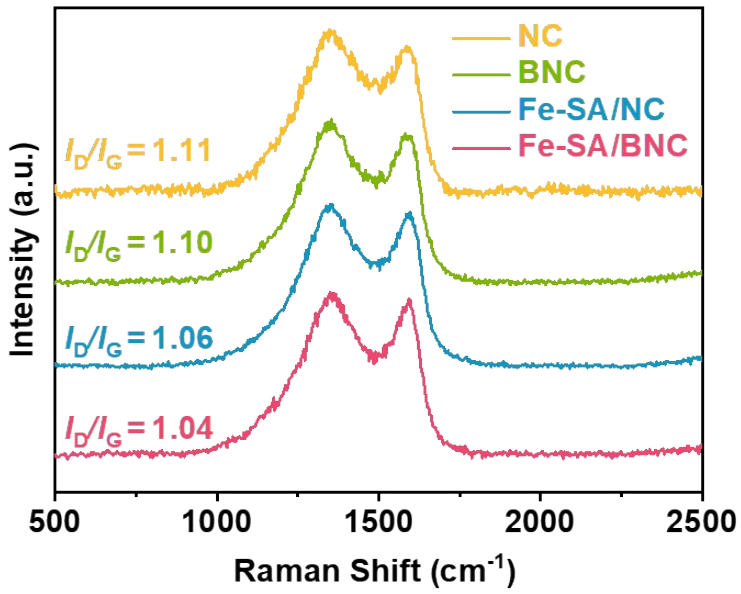

Fig. S9. Raman spectra of NC, BNC, Fe-SA/NC and Fe-SA/BNC.

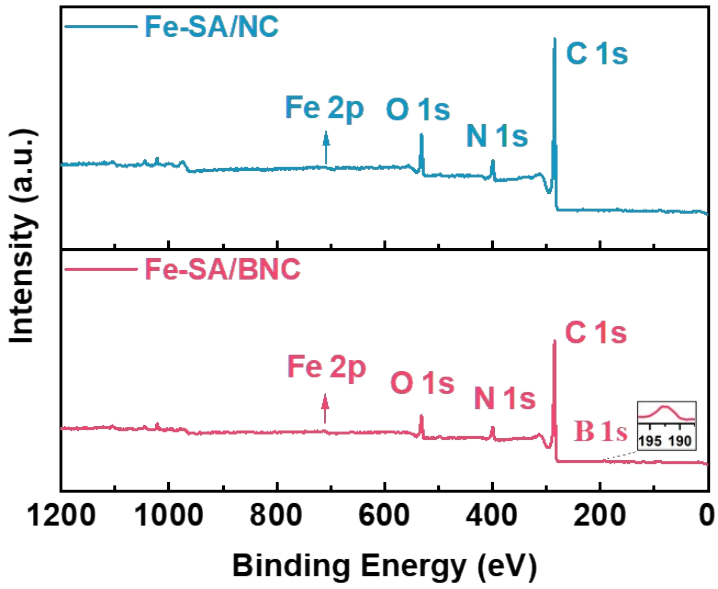

Fig. S10. XPS survey spectra of Fe-SA/NC and Fe-SA/BNC.

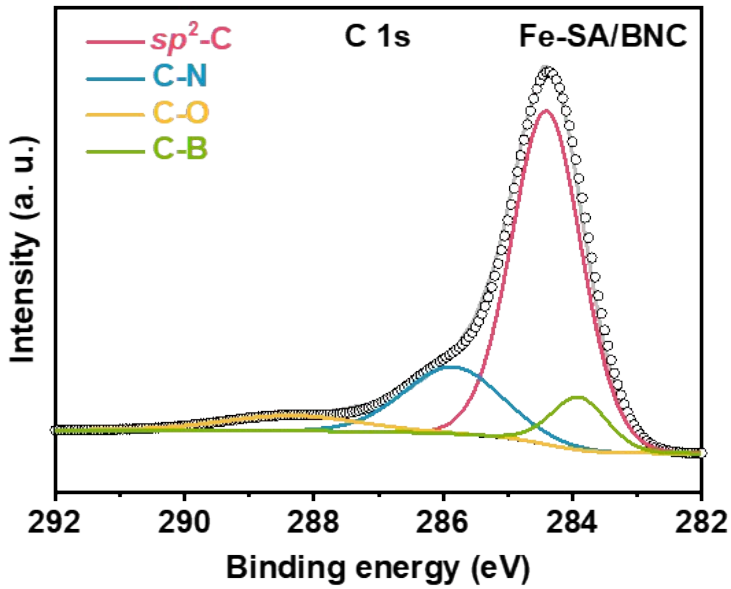

Fig. S11. High-resolution C 1s XPS spectrum for Fe-SA/BNC.

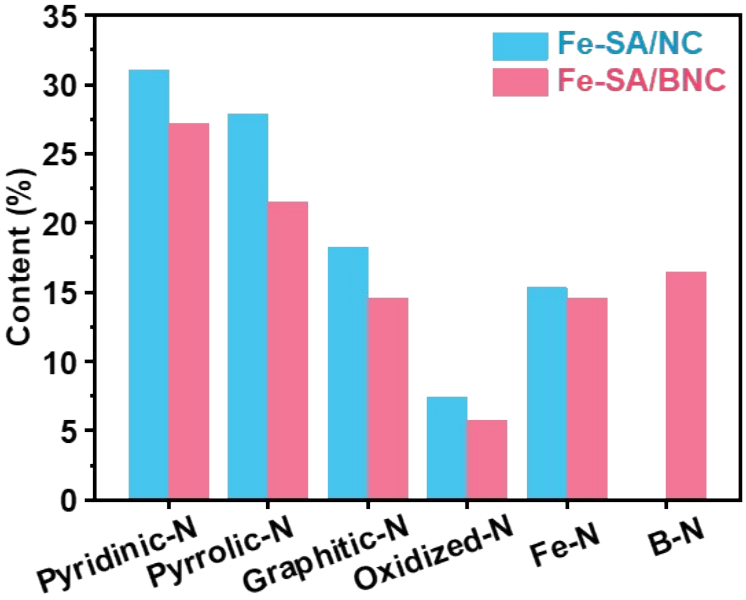

Fig. S12. Relative ratios of the deconvoluted peak areas of the N 1s XPS spectra for Fe-SA/NC and Fe-SA/BNC.

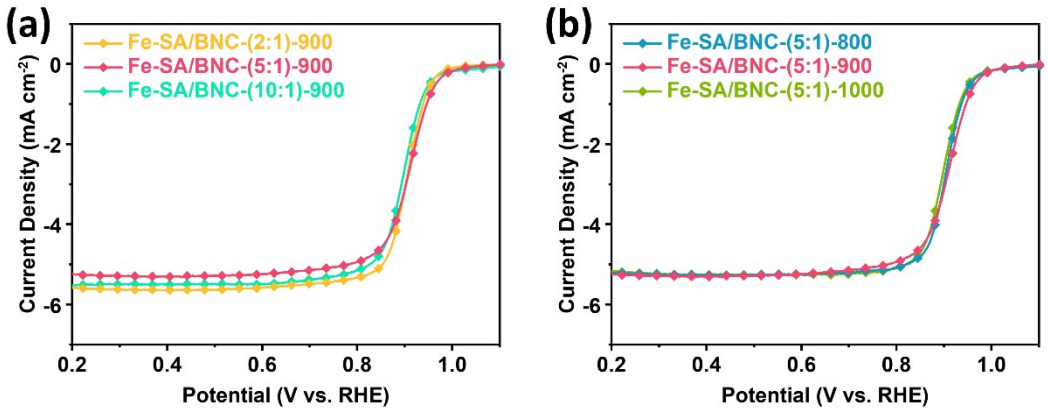

Fig. S13. (a) LSV curves of Fe-SA/BNC-(X)-900 at 1600 rpm (X represents the ratio of Fe-SA/NC to H_3BO_3). (b) LSV curves of Fe-SA/BNC-(5:1)-Y at 1600 rpm (Y represents the deposition temperature of B atoms). Fe-SA/BNC-(5:1)-900 was the optimal sample, abbreviated as Fe-SA/BNC.

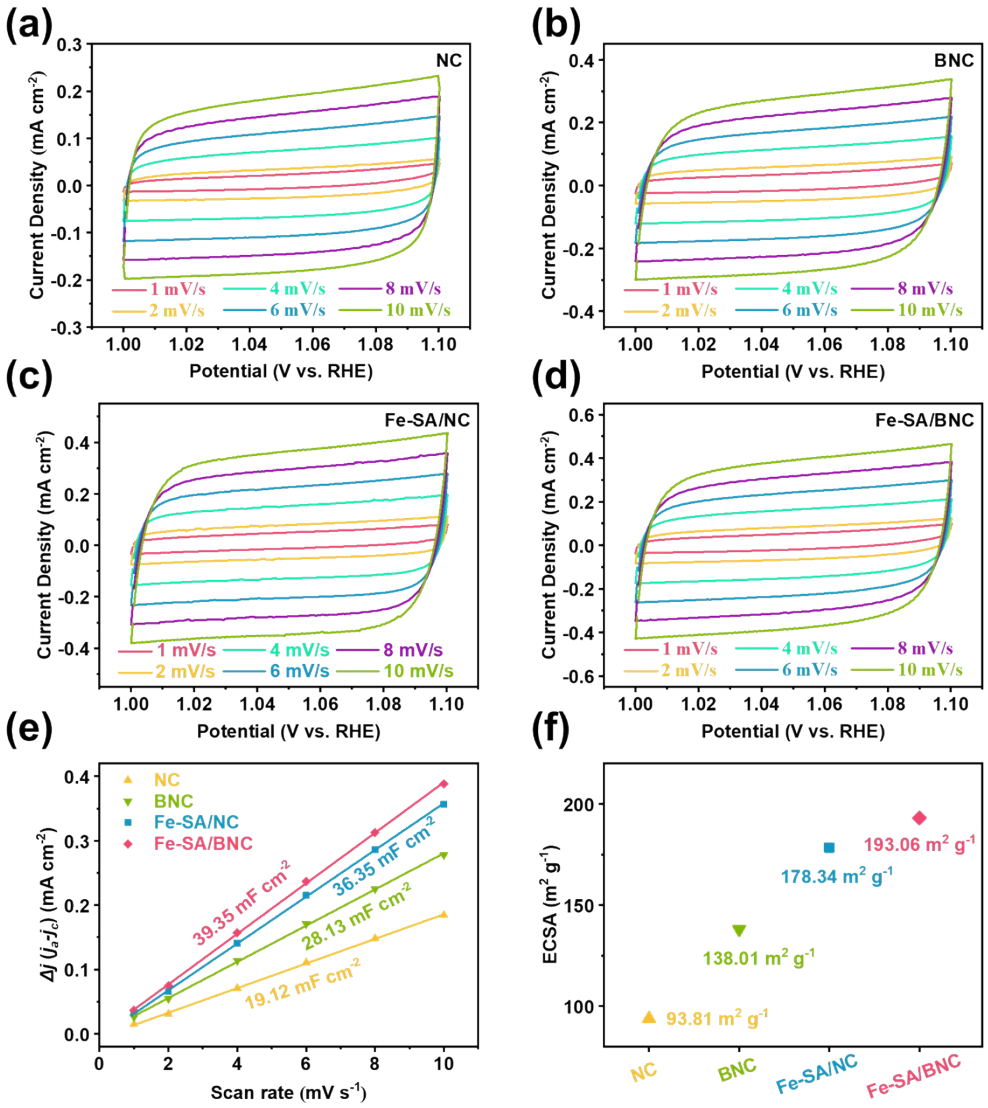

Fig. S14. CV curves of (a) NC, (b) BNC, (c) Fe-SA/NC and (d) Fe-SA/BNC at various scan rates. (e) The double-layer capacitances (C_{dl}) and (f) corresponding ECSA of NC, BNC, Fe-SA/NC and Fe-SA/BNC.

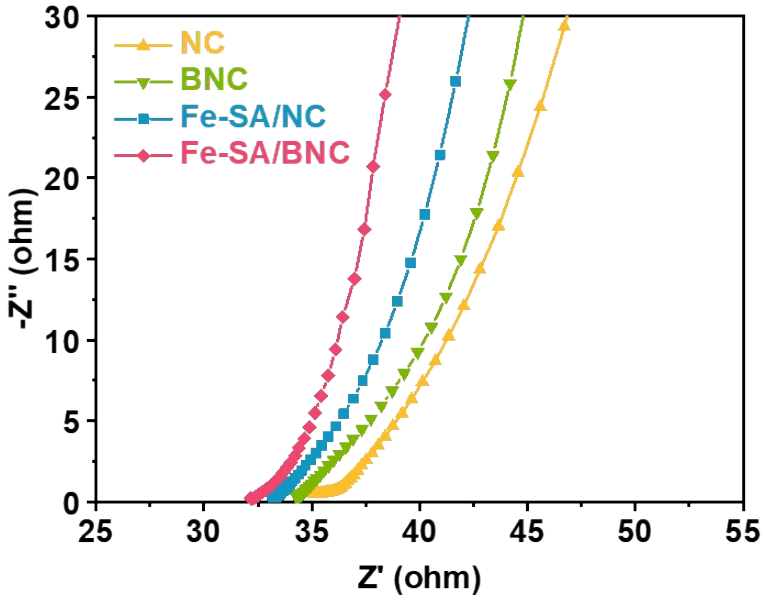

Fig. S15. Nyquist plots of NC, BNC, Fe-SA/NC and Fe-SA/BNC.

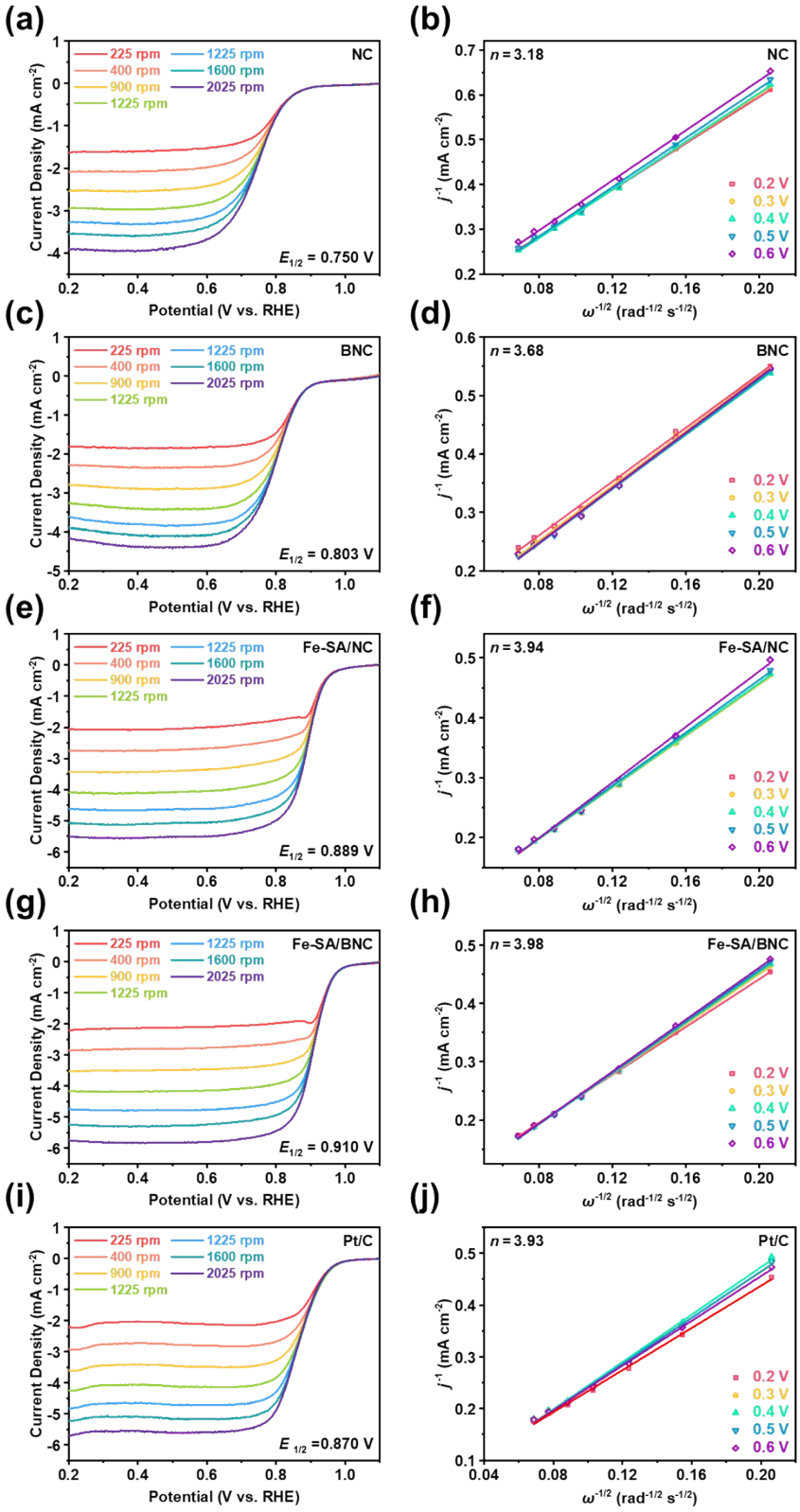

Fig. S16. LSV curves at different rotation rates and corresponding K-L plots of (a, b) NC, (c, d) BNC, (e, f) Fe-SA/NC, (g, h) Fe-SA/BNC and (i, j) Pt/C.

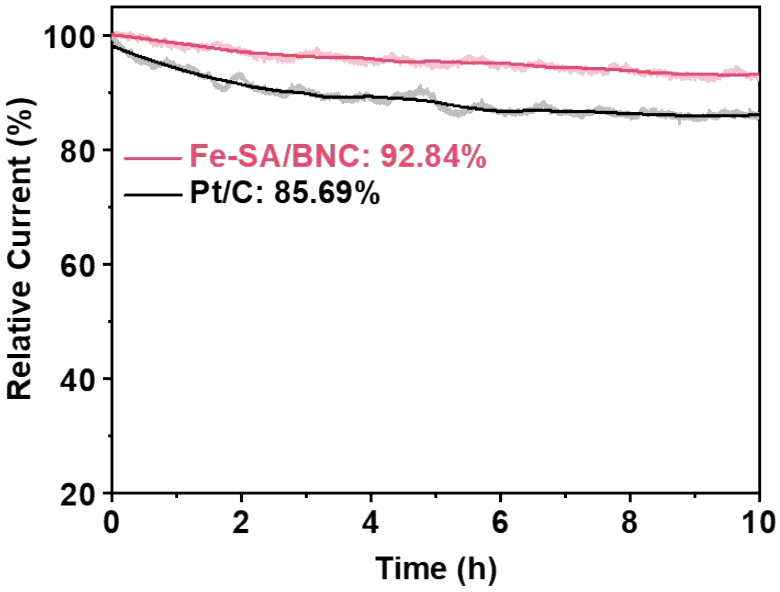

Fig. S17. Long-time chronoamperometric responses of Fe-SA/BNC and Pt/C at 0.4 V for 10 h.

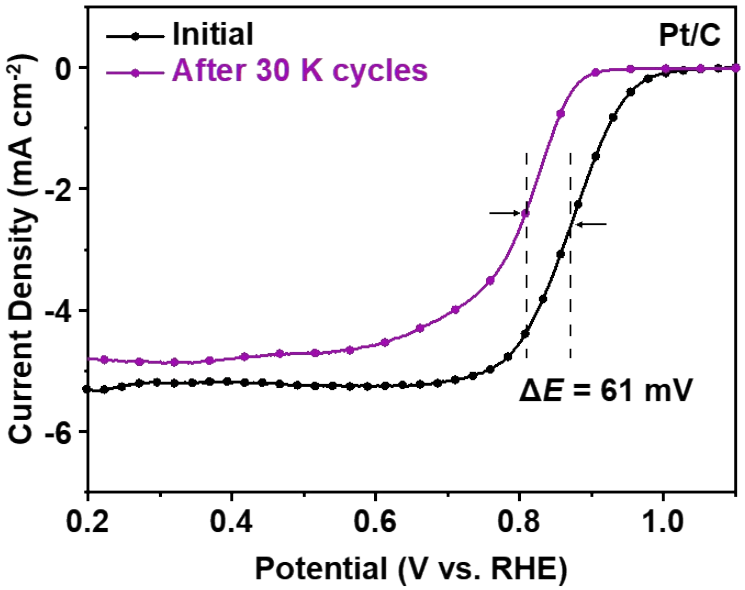

Fig. S18. LSV curves at 1600 rpm of Pt/C before and after 30 K cycles between 0.6 and 1.0 V with a scan rate of 200 mV s^{-1} at 1600 rpm.

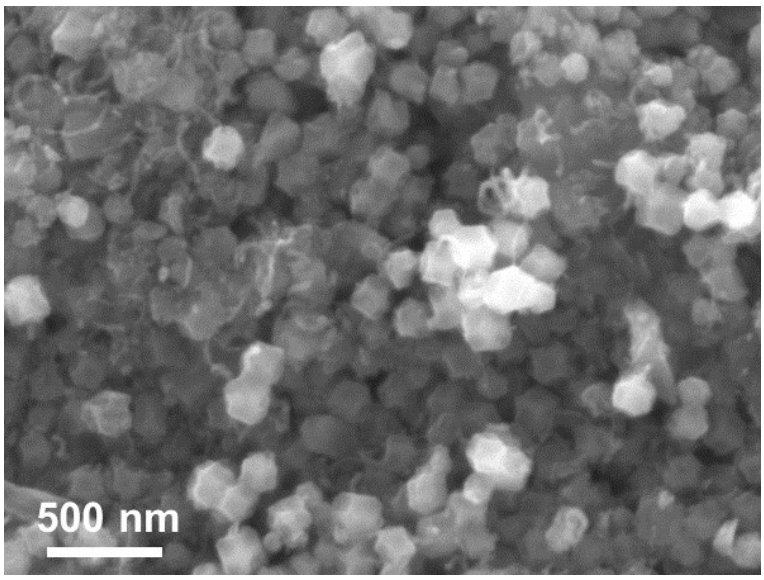

Fig. S19. SEM image of Fe-SA/BNC after 30 K cycles.

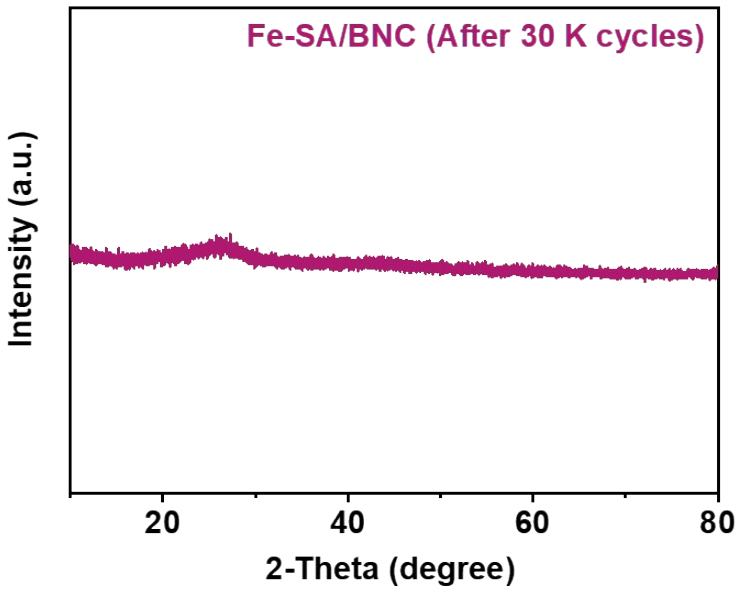

Fig. S20. XRD pattern of Fe-SA/BNC after 30 K cycles.

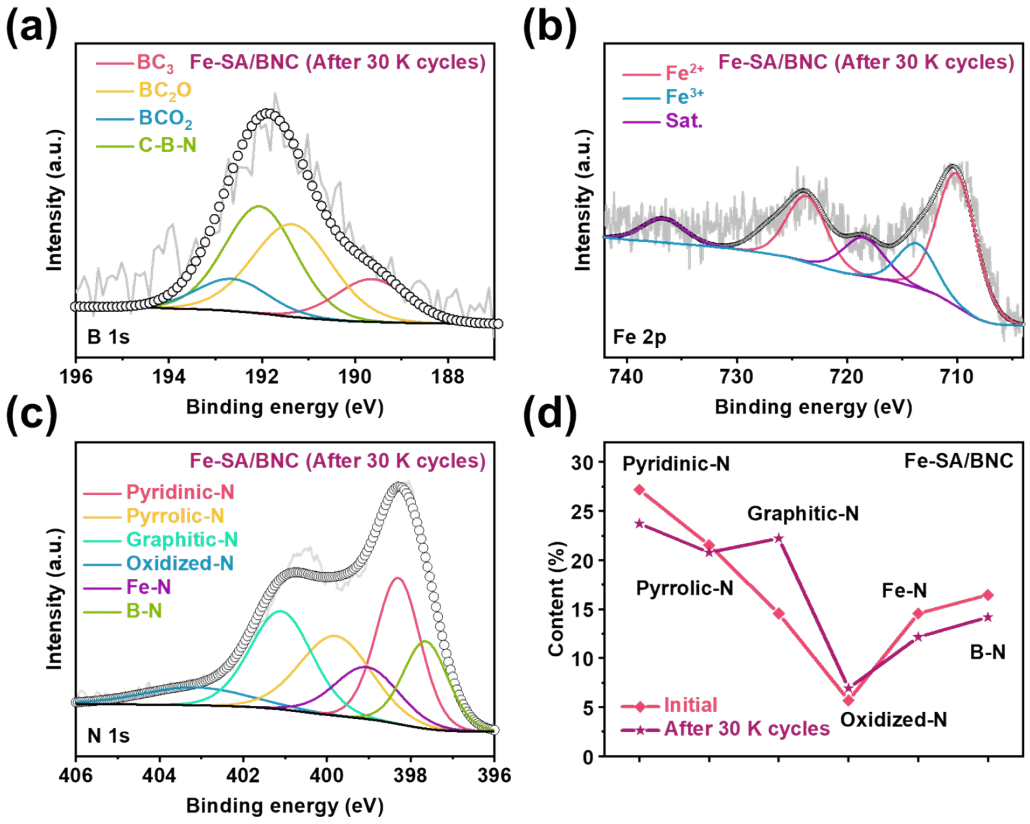

Fig. S21. High-resolution (a) B 1s, (b) Fe 2p and (c) N 1s XPS spectra for Fe-SA/BNC after 30 K cycles. (d) Relative ratios of the deconvoluted peak areas of the N 1s XPS spectra for Fe-SA/BNC before and after 30 K cycles.

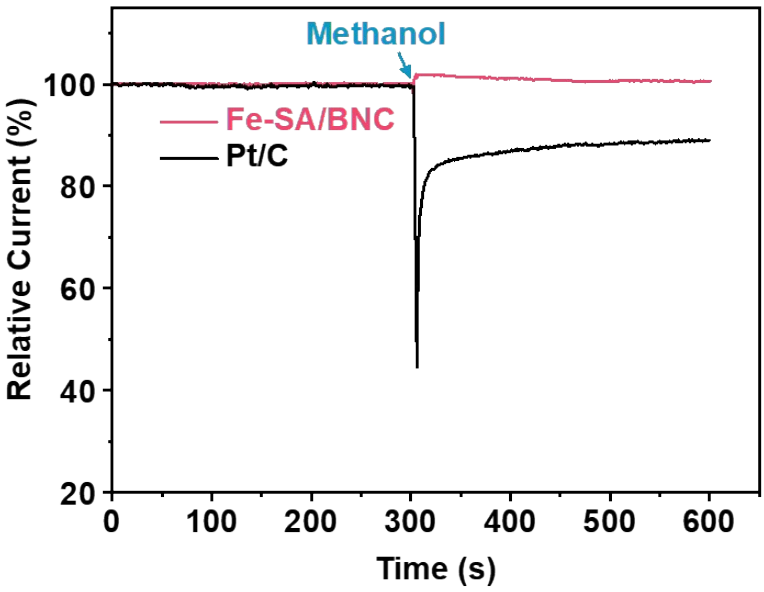

Fig. S22. Chronoamperometric response of Fe-SA/BNC and Pt/C with addition of 5 mL methanol after 300 s.

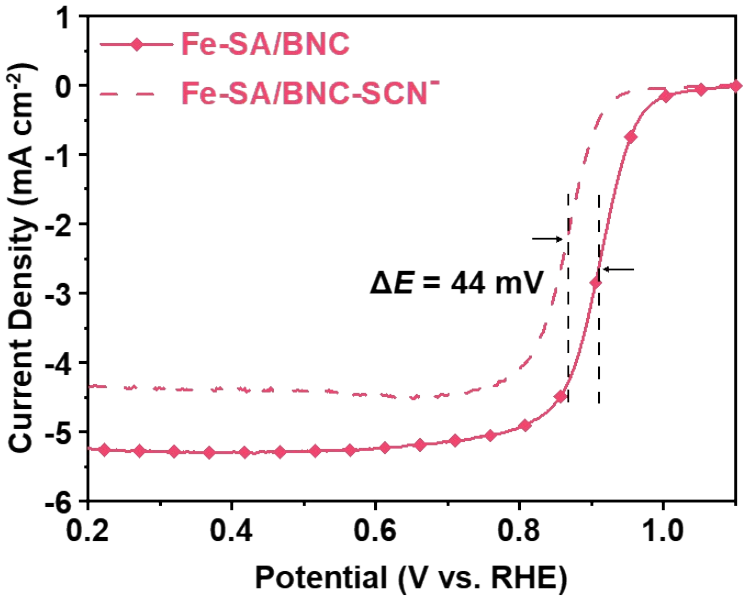

Fig. S23. LSV cures of Fe-SA/BNC with and without 10 mM KSCN in 0.1 M KOH.

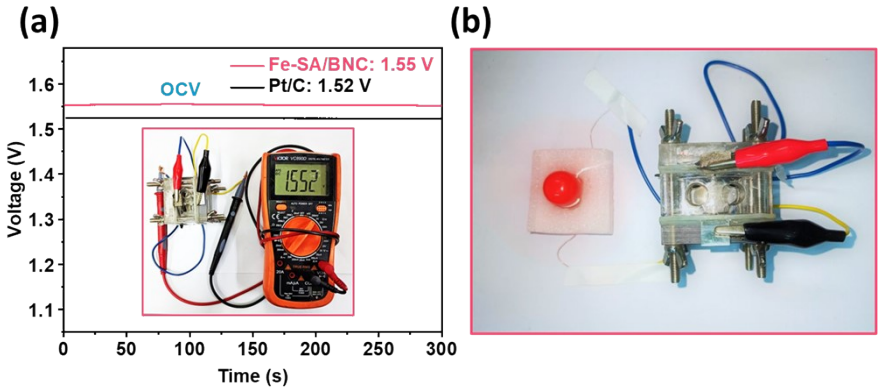

Fig. S24. (a) Open-circuit voltage (OCV) of liquid ZABs assembled with Fe-SA/BNC and Pt/C as the air cathode catalysts. Inset: photograph of liquid ZAB based on Fe-SA/BNC showing the OCV of 1.552 V. (b) Photograph of an electric fan powered by one liquid ZAB based on Fe-SA/BNC.

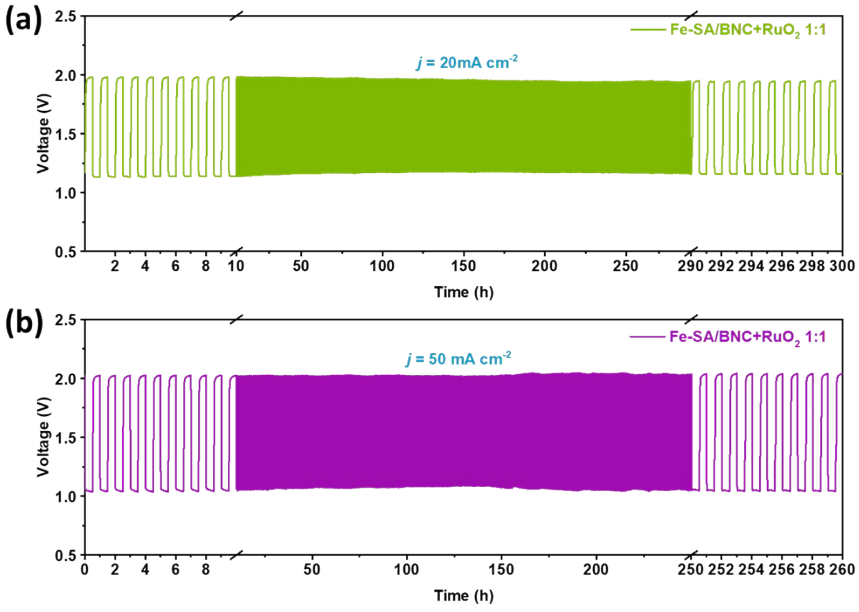

Fig. S25. (a, b) Long-time charge-discharge cycling curves of liquid ZAB assembled with Fe-SA/BNC+RuO_2 at the current densities of 20 mA cm^{-2} and 50 mA cm^{-2}.

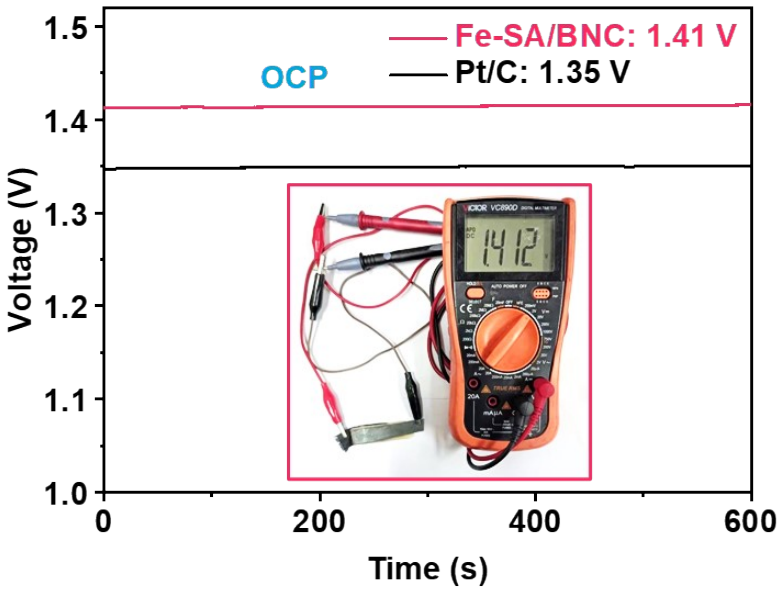

Fig. S26. Open-circuit voltage (OCV) of flexible solid-state ZABs assembled with Fe-SA/BNC and Pt/C as the air cathode catalysts. Inset: photograph of one flexible ZAB based on Fe-SA/BNC showing the OCV of 1.412 V.

Fig. S27. Photographs of a timer powered by one flexible solid-state ZAB based on Fe-SA/BNC under different bending degrees.

Table S1. Summary of the Brunauer–Emmett-Teller (BET) surface area and pore size distribution for Fe-SA/NC and Fe-SA/BNC.

Sample	BET surface area (m^2 g^{-1})	Micropore volume (cc g^{-1})	Mesopore volume (cc g^{-1})	Macropore volume (cc g^{-1})
Fe-SA/NC	769	0.225	0.521	0.320
Fe-SA/BNC	809	0.256	0.273	0.378

*Micropore and mesopore were determined using quenched solid density functional theory (QSDFT) method, while the macropore was determined using Barrett-Joyner-Halenda (BJH) method.

Table S2. Elemental contents of C, N, O, B and Fe based on XPS analysis for Fe-SA/NC, Fe-SA/BNC and Fe-SA/BNC after cycles.

Sample	Chemical composition (at%)				
	C	N	O	B	Fe
Fe-SA/NC	82.78	8.24	8.62	/	0.36
Fe-SA/BNC	82.18	7.59	6.64	3.21	0.38
Fe-SA/BNC (after cycles)	83.34	6.31	7.37	2.66	0.32

Table S3. EXAFS fitting parameters of Fe-SA/NC and Fe-SA/BNC.

Sample	Path	*N*	*R* (Å)	σ^2 (10^{-3}Å^2)	*R*-factor
Fe-SA/NC	Fe-N	3.9	1.98	5.0	0.05
Fe-SA/BNC	Fe-N	4.3	2.04	1.7	0.13

**N*, coordination number; *R*, distance between absorber and backscatter atoms; σ^2, Debye–Waller factor to account for both thermal and structural disorders; *R*-factor (%) indicates the goodness of the fit.

Table S4. Comparison of ORR performance of Fe-SA/BNC with previously reported advanced single-atom catalysts in alkaline solution.

Sample	Electrolyte	E_{onset} (V vs. RHE)	$E_{1/2}$ (V vs. RHE)	References
Fe-SA/BNC	**0.1 M KOH**	**1.02**	**0.910**	**This work**
Fe-CNG	0.1 M KOH	/	0.890	1
Fe/N-G-SAC	0.1 M KOH	/	0.890	2
Fe@NMC-1	0.1 M KOH	1.01	0.880	3
FeN_4Cl_1/NC	0.1 M KOH	/	0.910	4
Fe-SA-NSFC	0.1 M KOH	1.01	0.910	5
Fe(Fc)-N/S-C	0.1 M KOH	0.991	0.872	6
FeN4CB	0.1 M KOH	/	0.840	7
FeBNC-800	0.1 M KOH	0.968	0.838	8
Co-SAs@NC	0.1 M KOH	0.96	0.820	9
NC-Co SA	1 M KOH	1.00	0.870	10
Co-pyridinic N-C	0.1 M KOH	0.99	0.870	11
Co_1-N_3PS/HC	0.1 M KOH	1.00	0.920	12
CoSA/N,S-HCS	0.1 M KOH	0.96	0.850	13
Co-N/S-DSHCN-3.5	0.1 M KOH	0.989	0.878	14
Co-N,B-CSs	0.1 M KOH	/	0.830	15
Zn-B/N-C	0.1 M KOH	/	0.886	16
Se@NC-1000	0.1 M KOH	0.95	0.850	17
S-Cu-ISA/SNC	0.1 M KOH	1.05	0.918	18

Table S5. Comparison of open-circuit voltage, peak power density and specific capacities for liquid Zn-air batteries based on various reported electrocatalysts. All performances were reported in 6.0 M KOH.

Catalyst	Open-circuit voltage (V)	Peak power density (mW cm^{-2})	Specific capacities (mAh g^{-1}) @ mA cm^{-2}	References
Fe-SA/BNC	**1.55**	**308.3**	**819@50**	**This work**
D-Fe SAC	1.52	215	785@50	19
Fe/N,S-HC	1.46	239	809@10	20
Fe-NSDC	1.53	225.1	732@20	21
Fe/S_2-NC	1.51	170	/	22
Fe/SNCFs-NH_3	1.38	255.84	/	23
FeCoNi-NC	1.526	315.2	803.78@100	24
Co/CNWs/CNFs	1.46	304	823@5	25
OLC/Co-N-C	1.48	238	790@20	26
CoSA/N,S-HCS	1.50	173.1	781.1@10	13
Co_1-N_3PS/HC	1.47	176	786@10	12
CoSA+Co_9S_8/HCNT	1.45	177.33	788@100	27
B, N-Co/ CNs		93.93	727.5@10	28
Ni-N-C	1.462	178	827@5	29
Cu-SAs@N-CNS	/	192	856@20	30
□α-MoC/NHPC	1.44	200.3	783.9@10	31

References

1. W. Wan, Y. Zhao, S. Wei, C. A. Triana, J. Li, A. Arcifa, C. S. Allen, R. Cao and G. R. Patzke, Mechanistic insight into the active centers of single/dual-atom Ni/Fe-based oxygen electrocatalysts, *Nat. Commun.*, 2021, **12**, 5589.

2. M. Xiao, Z. Xing, Z. Jin, C. Liu, J. Ge, J. Zhu, Y. Wang, X. Zhao and Z. Chen, Preferentially Engineering FeN_4 Edge Sites onto Graphitic Nanosheets for Highly Active and Durable Oxygen Electrocatalysis in Rechargeable Zn-Air Batteries, *Adv. Mater.*, 2020, **32**, 2004900.

3. X. Chen, N. Wang, K. Shen, Y. Xie, Y. Tan and Y. Li, MOF-Derived Isolated Fe Atoms Implanted in N-Doped 3D Hierarchical Carbon as an Efficient ORR Electrocatalyst in Both Alkaline and Acidic Media, *ACS Appl. Mater. Interfaces*, 2019, **11**, 25976-25985.

4. L. Hu, C. Dai, L. Chen, Y. Zhu, Y. Hao, Q. Zhang, L. Gu, X. Feng, S. Yuan, L. Wang and B. Wang, Metal-Triazolate-Framework-Derived FeN_4Cl_1 Single-Atom Catalysts with Hierarchical Porosity for the Oxygen Reduction Reaction, *Angew. Chem. Int. Ed.*, 2021, **60**, 27324-27329.

5. Y. Zhou, X. Tao, G. Chen, R. Lu, D. Wang, M. X. Chen, E. Jin, J. Yang, H. W. Liang, Y. Zhao, X. Feng, A. Narita and K. Mullen, Multilayer stabilization for fabricating high-loading single-atom catalysts, *Nat. Commun.*, 2020, **11**, 5892.

6. X. H. Li, X. X. Yang, L. T. Liu, H. Zhao, Y. W. Li, H. Y. Zhu, Y. Z. Chen, S. W. Guo, Y. N. Liu, Q. Tan and G. Wu, Chemical Vapor Deposition for N/S-Doped Single Fe Site Catalysts for the Oxygen Reduction in Direct Methanol Fuel Cells, *ACS Catal.*, 2021, **11**, 7450-7459.

7. X. Zhao, X. Li, Z. Bi, Y. Wang, H. Zhang, X. Zhou, Q. Wang, Y. Zhou, H. Wang and G. Hu, Boron modulating electronic structure of FeN4C to initiate high-efficiency oxygen reduction reaction and high-performance zinc-air battery, *J. Energy Chem.*, 2022, **66**, 514-524.

8. K. Yuan, S. Sfaelou, M. Qiu, D. Lützenkirchen-Hecht, X. Zhuang, Y. Chen, C.

Yuan, X. Feng and U. Scherf, Synergetic Contribution of Boron and Fe–N_x Species in Porous Carbons toward Efficient Electrocatalysts for Oxygen Reduction Reaction, *ACS Energy Lett.*, 2017, **3**, 252-260.

9. X. Han, X. Ling, Y. Wang, T. Ma, C. Zhong, W. Hu and Y. Deng, Generation of Nanoparticle, Atomic-Cluster, and Single-Atom Cobalt Catalysts from Zeolitic Imidazole Frameworks by Spatial Isolation and Their Use in Zinc-Air Batteries, *Angew. Chem. Int. Ed.*, 2019, **58**, 5359-5364.

10. W. Zang, A. Sumboja, Y. Ma, H. Zhang, Y. Wu, S. Wu, H. Wu, Z. Liu, C. Guan, J. Wang and S. J. Pennycook, Single Co Atoms Anchored in Porous N-Doped Carbon for Efficient Zinc−Air Battery Cathodes, *ACS Catal.*, 2018, **8**, 8961-8969.

11. Y. Ha, B. Fei, X. Yan, H. Xu, Z. Chen, L. Shi, M. Fu, W. Xu and R. Wu, Atomically Dispersed Co‐Pyridinic N‐C for Superior Oxygen Reduction Reaction, *Adv. Energy Mater.*, 2020, **10**, 2002592.

12. Y. Chen, R. Gao, S. Ji, H. Li, K. Tang, P. Jiang, H. Hu, Z. Zhang, H. Hao, Q. Qu, X. Liang, W. Chen, J. Dong, D. Wang and Y. Li, Atomic-Level Modulation of Electronic Density at Cobalt Single-Atom Sites Derived from Metal-Organic Frameworks: Enhanced Oxygen Reduction Performance, *Angew. Chem. Int. Ed.*, 2021, **60**, 3212-3221.

13. Z. Zhang, X. Zhao, S. Xi, L. Zhang, Z. Chen, Z. Zeng, M. Huang, H. Yang, B. Liu, S. J. Pennycook and P. Chen, Atomically Dispersed Cobalt Trifunctional Electrocatalysts with Tailored Coordination Environment for Flexible Rechargeable Zn‐Air Battery and Self‐Driven Water Splitting, *Adv. Energy Mater.*, 2020, **10**, 2002896.

14. T. Wang, C. Yang, Y. Liu, M. Yang, X. Li, Y. He, H. Li, H. Chen and Z. Lin, Dual-Shelled Multidoped Hollow Carbon Nanocages with Hierarchical Porosity for High-Performance Oxygen Reduction Reaction in Both Alkaline and Acidic Media, *Nano Lett.*, 2020, **20**, 5639-5645.

15. Y. Guo, P. Yuan, J. Zhang, Y. Hu, I. S. Amiinu, X. Wang, J. Zhou, H. Xia, Z.

Song, Q. Xu and S. Mu, Carbon Nanosheets Containing Discrete Co-N_x-B_y-C Active Sites for Efficient Oxygen Electrocatalysis and Rechargeable Zn-Air Batteries, *ACS Nano*, 2018, **12**, 1894-1901.

16. J. Wang, H. Li, S. Liu, Y. Hu, J. Zhang, M. Xia, Y. Hou, J. Tse, J. Zhang and Y. Zhao, Turning on Zn 4s Electrons in a N_2-Zn-B_2 Configuration to Stimulate Remarkable ORR Performance, *Angew. Chem. Int. Ed.*, 2021, **60**, 181-185.

17. H. Hu, J. Wang, B. Cui, X. Zheng, J. Lin, Y. Deng and X. Han, Atomically Dispersed Selenium Sites on Nitrogen-Doped Carbon for Efficient Electrocatalytic Oxygen Reduction, *Angew. Chem. Int. Ed.*, 2022, **61**, 202114441.

18. H. Shang, X. Zhou, J. Dong, A. Li, X. Zhao, Q. Liu, Y. Lin, J. Pei, Z. Li, Z. Jiang, D. Zhou, L. Zheng, Y. Wang, J. Zhou, Z. Yang, R. Cao, R. Sarangi, T. Sun, X. Yang, X. Zheng, W. Yan, Z. Zhuang, J. Li, W. Chen, D. Wang, J. Zhang and Y. Li, Engineering unsymmetrically coordinated Cu-S_1N_3 single atom sites with enhanced oxygen reduction activity, *Nat. Commun.*, 2020, **11**, 3049.

19. J. Yang, Z. Wang, C. X. Huang, Y. Zhang, Q. Zhang, C. Chen, J. Du, X. Zhou, Y. Zhang, H. Zhou, L. Wang, X. Zheng, L. Gu, L. M. Yang and Y. Wu, Compressive Strain Modulation of Single Iron Sites on Helical Carbon Support Boosts Electrocatalytic Oxygen Reduction, *Angew. Chem. Int. Ed.*, 2021, **60**, 22722-22728.

20. F. Liu, L. Shi, S. Song, K. Ge, X. Zhang, Y. Guo and D. Liu, Simultaneously Engineering the Coordination Environment and Pore Architecture of Metal-Organic Framework-Derived Single-Atomic Iron Catalysts for Ultraefficient Oxygen Reduction, *Small*, 2021, **17**, 2102425.

21. J. Zhang, M. Zhang, Y. Zeng, J. Chen, L. Qiu, H. Zhou, C. Sun, Y. Yu, C. Zhu and Z. Zhu, Single Fe Atom on Hierarchically Porous S, N-Codoped Nanocarbon Derived from Porphyra Enable Boosted Oxygen Catalysis for Rechargeable Zn-Air Batteries, *Small*, 2019, **15**, 1900307.

22. H. Jin, X. Zhao, L. Liang, P. Ji, B. Liu, C. Hu, D. He and S. Mu, Sulfate Ions Induced Concave Porous S-N Co-Doped Carbon Confined FeC_x Nanoclusters with Fe-

N_4 Sites for Efficient Oxygen Reduction in Alkaline and Acid Media, *Small*, 2021, **17**, 2101001.

23. L. Yang, X. Zhang, L. Yu, J. Hou, Z. Zhou and R. Lv, Atomic Fe-N_4 /C in Flexible Carbon Fiber Membrane as Binder-Free Air Cathode for Zn-Air Batteries with Stable Cycling over 1000 h, *Adv. Mater.*, 2022, **34**, 2105410.

24. X. Tang, R. Cao, L. Li, B. Huang, W. Zhai, K. Yuan and Y. Chen, Engineering efficient bifunctional electrocatalysts for rechargeable zinc–air batteries by confining Fe–Co–Ni nanoalloys in nitrogen-doped carbon nanotube@nanosheet frameworks, *J. Mater. Chem. A*, 2020, **8**, 25919-25930.

25. C. Xia, L. Huang, D. Yan, A. I. Douka, W. Guo, K. Qi and B. Y. Xia, Electrospinning Synthesis of Self‐Standing Cobalt/Nanocarbon Hybrid Membrane for Long‐Life Rechargeable Zinc–Air Batteries, *Adv. Funct. Mater.*, 2021, **31**, 2105021.

26. Z. Liang, N. Kong, C. Yang, W. Zhang, H. Zheng, H. Lin and R. Cao, Highly Curved Nanostructure-Coated Co, N-Doped Carbon Materials for Oxygen Electrocatalysis, *Angew. Chem. Int. Ed.*, 2021, **60**, 12759-12764.

27. Y. Li, R. Cao, L. Li, X. Tang, T. Chu, B. Huang, K. Yuan and Y. Chen, Simultaneously Integrating Single Atomic Cobalt Sites and Co_9S_8 Nanoparticles into Hollow Carbon Nanotubes as Trifunctional Electrocatalysts for Zn-Air Batteries to Drive Water Splitting, *Small*, 2020, **16**, 1906735.

28. W. J. Niu, Q. Q. Sun, Y. P. Wang, B. N. Gu, M. J. Liu, J. Z. He, J. L. Chen, C. C. Chung, W. W. Liu and Y. L. Chueh, Design of Co Nanoparticles‐Encapsulated by Boron and Nitrogen Co‐Doped Carbon Nanosheets as Highly Efficient Electrocatalyst for Oxygen Reduction Reaction, *Adv. Mater. Interfaces*, 2021, **8**, 2101454.

29. S. Zhang, H. Xue, W. L. Li, J. Sun, N. Guo, T. Song, H. Dong, J. Zhang, X. Ge, W. Zhang and Q. Wang, Constructing Precise Coordination of Nickel Active Sites on

Hierarchical Porous Carbon Framework for Superior Oxygen Reduction, *Small*, 2021, **17**, 2102125.

30. L. Zong, K. Fan, W. Wu, L. Cui, L. Zhang, B. Johannessen, D. Qi, H. Yin, Y. Wang, P. Liu, L. Wang and H. Zhao, Anchoring Single Copper Atoms to Microporous Carbon Spheres as High‐Performance Electrocatalyst for Oxygen Reduction Reaction, *Adv. Funct. Mater.*, 2021, **31**, 2104864.

31. G. Chen, T. Wang, P. Liu, Z. Liao, H. Zhong, G. Wang, P. Zhang, M. Yu, E. Zschech, M. Chen, J. Zhang and X. Feng, Promoted oxygen reduction kinetics on nitrogen-doped hierarchically porous carbon by engineering proton-feeding centers, *Energy Environ. Sci.*, 2020, **13**, 2849-2855.